



Cite this: DOI: 10.1039/c5nr07019h

Received 10th October 2015,  
Accepted 26th December 2015

DOI: 10.1039/c5nr07019h

www.rsc.org/nanoscale

Direct *in situ* observation of ZnO nucleation and growth *via* transmission X-ray microscopy†S. E. R. Tay,<sup>‡a</sup> A. E. Goode,<sup>‡a</sup> J. Nelson Weker,<sup>b</sup> A. A. Cruickshank,<sup>a</sup> S. Heutz,<sup>a</sup>  
A. E. Porter,<sup>a</sup> M. P. Ryan<sup>\*a</sup> and M. F. Toney<sup>b</sup>

The nucleation and growth of a nanostructure controls its size and morphology, and ultimately its functional properties. Hence it is crucial to investigate growth mechanisms under relevant growth conditions at the nanometer length scale. Here we image the nucleation and growth of electrodeposited ZnO nanostructures *in situ*, using a transmission X-ray microscope and specially designed electrochemical cell. We show that this imaging technique leads to new insights into the nucleation and growth mechanisms in electrodeposited ZnO including direct, *in situ* observations of instantaneous *versus* delayed nucleation.

Electrodeposition (ED) is an attractive method for the synthesis of supported nanoparticles and nanostructured coatings.<sup>1</sup> ED provides the advantages of scalability and low operational costs. It is extremely versatile both in terms of the materials that can be processed (metals, ceramics and polymers) and the ability to control nanoparticle size and morphology using deposition conditions such as electrolyte composition, deposition potential, temperature, deposition time and pH.<sup>1</sup> The size and morphology of the synthesized nanoparticles determines their properties, and is strongly dependent on nanoparticle nucleation and growth. Therefore, there is a need for advanced methods to observe nanoparticle nucleation and growth *in situ*, and on the nanometre length scale. With a deeper understanding of nucleation and growth, devices with improved crystallinity and tailored texturing could be deposited with optimised or enhanced properties.

Few techniques are capable of providing spatially resolved information on nanostructure growth *in situ*. Transmission electron microscopy (TEM) and synchrotron-based transmission X-ray microscopy (TXM) are two techniques which probe structure and chemistry at the nanometre scale.

Recently, wet-cells have been developed whereby a liquid sample is contained between two membranes, often SiN<sub>x</sub> windows, allowing studies of growth process in liquid environments to be conducted within these microscopes. The wet cells have to meet the fundamental requirement of electron or X-ray transmission. This requirement limits the dimensions of an *in situ* TEM cell to the order of several hundred nanometres,<sup>2–4</sup> while X-ray microscopes offer more relaxed sample thickness constraints on the order of millimetres depending on the photon energy.<sup>5</sup> The most simple *in situ* cells involve small volumes of liquid sealed between two SiN<sub>x</sub> windows (see for example the study of ZnO precipitation in the TEM by Liu *et al.*,<sup>4</sup> or the *in situ* scanning transmission X-ray microscope (STXM) study of pH-induced structural changes in microgels by Fujii *et al.*<sup>6</sup>). Microfabrication techniques have also been used to add functionality to the cells. De Groot *et al.* utilised an in-built platinum heater on a SiN<sub>x</sub> window to observe a working catalyst *in situ* in a STXM, at temperatures up to 500 °C and at atmospheric pressure.<sup>7</sup> A three electrode cell has even been patterned on to SiN<sub>x</sub> windows by Williamson *et al.*<sup>8</sup> to study the nucleation and growth of electrodeposited Cu *in situ* in the TEM.

However, a significant problem in the use of sealed cells of restricted dimensions is that systems often experience diffusion-limited constraints. Such limitations may not be reflective of actual conditions in bulk, especially in the case of electrodeposition where the volume of a standard cell is many orders of magnitude larger than an *in situ* cell containing as little as 100 nL of liquid.<sup>9</sup> In fact, Williamson *et al.* report reduced growth rates of Cu clusters after just two seconds of electrodeposition in their *in situ* cell, attributed to a depletion of ions in the electrolyte. The addition of flow to SiN<sub>x</sub> cells, which reduces diffusion limitations, has been used for example by Rieger *et al.* in their TEM study of CaCO<sub>3</sub> precipitation<sup>10</sup> and by Wang *et al.* to observe galvanic replacement reactions between silver nanowires and HAuCl<sub>4</sub>.<sup>11</sup> Alternative strategies to develop larger cells for *in situ* hard X-ray microscopy have been less well explored. Recently, Nelson Weker *et al.*<sup>12,13</sup> developed a battery pouch cell capable of holding up to 5 µL of electrolyte,

<sup>a</sup>Department of Materials and London Centre for Nanotechnology, Imperial College London, Exhibition Road, London SW7 2AZ, UK. E-mail: m.p.ryan@imperial.ac.uk

<sup>b</sup>Stanford Synchrotron Radiation Lightsource, Stanford University, 2575 Sand Hill Road, Menlo Park, California 94025, USA

†Electronic supplementary information (ESI) available: Methods and videos of nanoparticle growth. See DOI: 10.1039/c5nr07019h

‡These authors contributed equally to this work.

to study morphological changes in lithium–sulfur batteries during cycling, in two and three dimensions.

In the study presented here, we develop an *in situ* three electrode cell capable of studying the electrodeposition of nanostructures within a transmission X-ray microscope. This cell is 3D printed, without microfabrication techniques, and capable of holding relatively large volumes (30 mL) of electrolyte. We demonstrate direct, *in situ* observations of the growth of electrodeposited nanostructures in the widely studied ZnO system. In this system, nanoparticle composition, morphology and film quality is controlled by varying the concentration of  $\text{Zn}^{2+}$  ions and the deposition potential.<sup>14</sup> To our knowledge, this study is the first to report direct *in situ* TXM imaging and analysis of electrodeposited nanomaterials; this approach will enable the observation of direct nucleation and growth mechanisms in other ED systems.

A customised cell (Fig. 1) was designed for electrodeposition and simultaneous X-ray imaging using the Carl Zeiss (formerly Xradia) full-field X-ray microscope at the Stanford Synchrotron Radiation Lightsource (SSRL) beamline 6–2. The cell contains ~30 mL of electrolyte and tapers to a width of 2 mm at the bottom, where the X-ray beam passes through two Kapton windows. One window was sputter-coated with 10 nm Au to form the working electrode. A Pt counter electrode and Ag/AgCl reference microelectrode are located above the windows, along with a resistive heater and pipette for bubbling  $\text{O}_2$ . This enabled imaging of ZnO nanostructures deposited under a range of conditions to yield different nanostructure morphologies. The electrolyte contained  $\text{Zn}(\text{NO}_3)_2$  concentrations of 5 mM or 50 mM, with 0.1 M of KCl as supporting electrolyte. Deposition potentials of  $-0.75$  V or  $-0.97$  V (vs. Ag/AgCl) were used, with  $\text{O}_2$  bubbling and a temperature of  $65^\circ\text{C}$ .

X-ray absorption images were recorded with 2.0 s exposure times, at intervals of 2.2 s during electrodeposition. Micrographs were acquired with spatial resolutions of ~30 nm using 9700 eV photons, just above the Zn K-edge (Fig. 2a–h). This

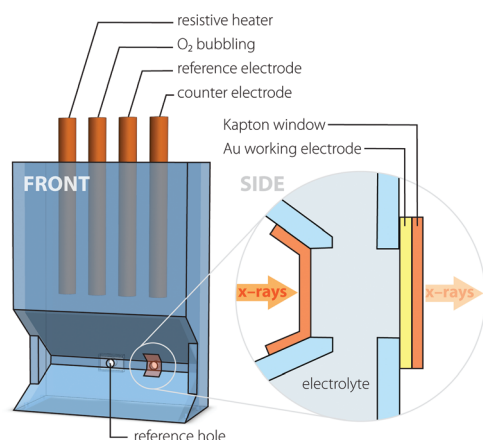


**Fig. 1** Schematic showing front and side views of *in situ* electrochemical cell. Inset shows the path of the X-ray beam through 2 mm of electrolyte and Kapton windows, one of which is sputter-coated with Au to act as the working electrode.

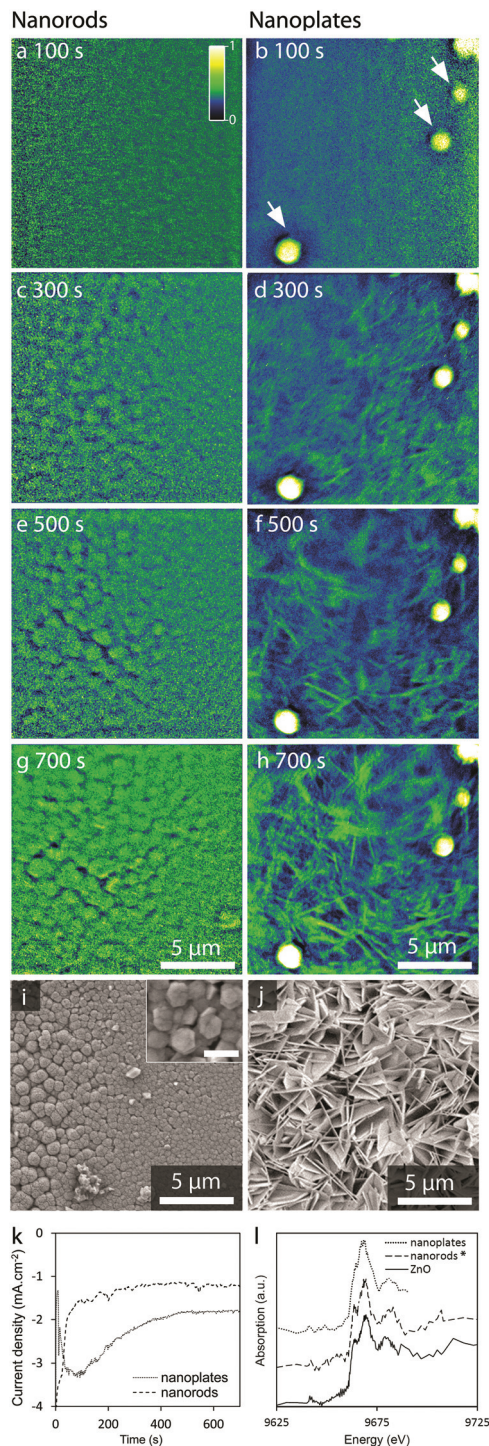


**Fig. 2** (a–h) False colour absorption images showing the evolution of nanoparticle morphology (thickest regions in green/yellow), and (i, j) *ex situ* SEM images acquired after deposition. Arrows in (b) mark Au fiducial markers. Scale bar in inset = 500 nm. Micrographs have been Fourier filtered to remove bright single-pixel artefacts (for unfiltered images see Fig. S1†). (k) Electrochemical current density, as a function of time during deposition, and (l) XANES characterisation of the final nanoparticle films. Experimental parameters are: 5 mM  $\text{Zn}(\text{NO}_3)_2$  for nanorods and 50 mM  $\text{Zn}(\text{NO}_3)_2$  for nanoplates. Deposition potential was  $-0.97$  V, or  $-0.75$  V where indicated (\*).



provided good absorption contrast for both ZnO nanostructures and also Au nanoparticle fiducial markers (arrows, Fig. 2b) on the back surface of the Au working electrode. These fiducial markers, which are present in nanoplate micrographs but cropped from the field of view of the nanorod micrographs in Fig. 2, were used for correction of drift between images and for focusing on the working electrode before starting ED. Absorption images from *in situ* depositions show the morphological evolution of nanorod and nanoplate films ( $-0.97$  V,  $5$  mM and  $50$  mM  $[\text{Zn}^{2+}]$  respectively; Fig. 2 and ESI videos 1, 2†). After  $100$  s, the main structures visible are only the Au fiducial markers. By  $300$  s, nanostructures with distinct morphologies are visible in the micrographs. In the nanorod sample, the structures grew bigger in diameter with time (Fig. 2e, g and S2†). In the case of nanoplates, the diameters increased with insignificant changes in plate thickness (Fig. 2f, h). As nanoplate evolution was dominated by an increase in nanostructure size rather than particle density, this strongly suggests an initial instantaneous nucleation phase followed by growth.

Fig. 2i and j show scanning electron microscope (SEM) characterisation of the same films after electrodeposition. The morphology of nanoplates in the electron micrographs closely matches the structures observed in TXM absorption images, as well as structures reported in the literature.<sup>15</sup> Note that for the nanorod sample, the features observed in X-ray micrographs are not individual nanorods but larger rounded structures  $0.7\text{--}1\text{ }\mu\text{m}$  in diameter which are also present on the left hand side of the SEM micrograph (Fig. 2i). This area had been exposed to a higher total X-ray dose, as thermal drift of the sample holder shifted the area of illumination during *in situ* deposition. The rounded structures observed in this work closely resemble ZnO pillars reported by Cembrero *et al.*,<sup>21</sup> which were formed during electrodeposition at an elevated temperature of  $80\text{ }^{\circ}\text{C}$ .

While individual nanorods were not resolved in X-ray micrographs, *ex situ* SEM imaging of the same sample revealed a densely packed nanorod film, with nanorods  $50\text{--}90$  nm in diameter (right hand side and inset of Fig. 2i). The inability of TXM to resolve these nanostructures is due to a combination of (a) the limited spatial resolution of the TXM, (b) the low signal to noise ratio of the dynamic imaging conditions and (c) the dense nature of the nanorod film, which provides little contrast in transmission mode. By comparison, secondary electron imaging in the SEM with its higher spatial resolution and sensitivity to surface topography is much better suited to characterising detailed resultant surface morphology.

*In situ* electrodeposition was also monitored using the cathodic current density (Fig. 2k). Initial peaks in the current density transients (at  $25$  s for nanorods and  $90$  s for nanoplates) are observed corresponding to the nucleation phase, followed by a steady current density which was larger in magnitude for the nanoplate film compared to the nanorod film. This higher current density is attributed to the increased Zn  $(\text{NO}_3)_2$  concentration, which leads to increased nitrate reduction (ESI eqn (2)†). X-ray absorption near edge structure

(XANES) spectra of the nanostructured films were recorded in transmission mode after electrodeposition on the same beam-line (Fig. 2l). Spectra are consistent with the formation of ZnO and Zn hydroxychloride, which are in agreement with previous experiments for ZnO nanostructured films respectively.<sup>16,17</sup>

Fig. 3 shows a series of absorption images acquired during electrodeposition using  $50$  mM  $[\text{Zn}^{2+}]$  and a less negative deposition potential of  $-0.75$  V. The current density displays a delayed and prominent peak between  $200$  and  $500$  s corresponding to a lengthy nucleation process (Fig. 3q). Between  $200$  s and  $350$  s, rapid changes in particle distribution are observed (Fig. 3a–p, ESI videos 3 and 4†). Structures sometimes appear blurred in one direction (*e.g.* horizontally in Fig. 3b), which is most likely due to movement of particles in the electrolyte during the  $2$  s acquisition time of each micrograph. By  $350$  s, the swirling particles were no longer observed. Particles remained stationary on the substrate and grew in size (ESI video 3†), apart from a cluster of particles which changed position suddenly  $\sim 450$  s into deposition. These observations are

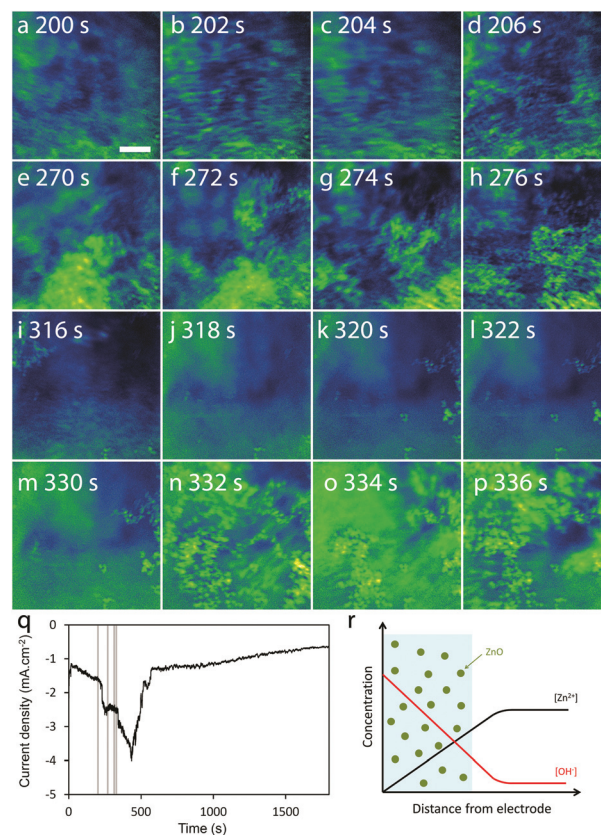


**Fig. 3** (a–p) Absorption images in each row were acquired 2.2 seconds apart, at  $\sim 200$  s (a–d),  $270$  s (e–h),  $315$  s (i–l) and  $330$  s (m–p). Swirling particles which appear smeared out are most apparent in (a–d) and are also present at later times (n–p). See ESI video 3.† (q) Electrochemical current density, as a function of time during deposition. Vertical lines correspond to timings of micrographs in a–p. Experimental parameters:  $50$  mM  $\text{Zn}(\text{NO}_3)_2$ , deposition potential  $-0.75$  V. (r) Schematic of local area close to working electrode with ZnO (in green) precipitation due to supersaturation of ZnO at high hydroxyl concentration. Scale bar  $5\text{ }\mu\text{m}$ .

consistent with the nucleation of ZnO precipitates within the electrolyte close to the electrode surface. As the blurred particles appear to be in focus (without defocus fringes), we can conclude that they are located within  $\sim 50\ \mu\text{m}$  of the working electrode surface. In the vicinity of the working electrode, the hydroxyl concentration is increasing due to nitrate reduction and the solubility limit of ZnO is reached (Fig. 3r).<sup>14,18</sup> ZnO is hypothesised to precipitate in the electrolyte and subsequently become deposited onto the electrode where it continues to grow. This observation of 'swirling' at the less negative potential of  $-0.75\ \text{V}$  and not at  $-0.97\ \text{V}$  is consistent with the increased reaction rate for nitrate reduction at more negative potentials, and the resultant rapid supersaturation and nucleation directly at the electrode surface: hence precipitates are stationary at the substrate at much faster time scales. This direct, *in situ* observation of instantaneous *versus* delayed nucleation highlights the advantage of using TXM to understand dynamic processes in nucleation and growth studies.

Prior to this work, *in situ* studies of ZnO nanostructure growth were performed using X-ray diffraction and bulk XANES,<sup>16,19</sup> and imaging on the nanometre length scale could only be achieved by analysing films *ex situ* using SEM.<sup>19</sup> However, it is well known that ZnO can re-dissolve into the electrolyte once the applied field is removed and  $\text{OH}^-$  diffusion away from the electrode restores the system pH.<sup>20</sup> Artefacts may arise due to partial dissolution of nanostructures between the end of electrodeposition and the removal of the substrate from the electrolyte. Small nanostructures which form at the start of the nucleation process will be particularly affected by dissolution, making their size and morphology difficult to measure by *ex situ* electron microscopy. Here, the ability to image nanostructures through the surrounding electrolyte and under applied field during deposition allows avoidance of dissolution, adhesion or drying artefacts. However, the difficulty of imaging 50–90 nm nanorods in this work illustrates the current limitations of *in situ* TXM in resolving the smallest nanostructures formed at the start of nucleation. Future improvements in X-ray optics and imaging methodologies will be necessary to extend this *in situ* analysis towards earlier nucleation events. Furthermore for a given X-ray source, the temporal resolution, signal-to-noise ratio (SNR) and delivered dose represent orthogonal constraints which need to be optimised based on the analytical requirements in question. This limitation could be partially overcome by employing (brighter) X-ray free electron laser (XFEL) sources capable of delivering femtosecond temporal resolution without reducing the SNR. In either case, a detailed understanding of the effects of X-ray irradiation on *in situ* nanoparticle nucleation and growth is required to minimise or avoid altering these dynamic processes.

## Conclusions

We have demonstrated with TXM *in situ* X-ray microscopy imaging of the nucleation and growth of ZnO nanorods and

nanoplates. At  $-0.97\ \text{V}$ , real-time growth of nanorods and nanoplates were observed at 5 mM and 50 mM of  $[\text{Zn}^{2+}]$  respectively. New nucleation sites were not observed, indicating an initial instantaneous nucleation followed by growth. Image stills at various time points highlighted morphological changes during growth. In contrast, at  $-0.75\ \text{V}$ , solution supersaturation events are observed, with swirling of ZnO particles in the electrolyte. Our results are consistent with established understanding in literature regarding ZnO precipitation at supersaturated conditions, which has been long hypothesised but not experimentally verified or visualised until now. These transient events which occur away from the substrate surface cannot be accessed using conventional *ex situ* techniques. However, given the current limitations on X-ray resolution, correlation between *ex situ* electron microscopy analysis and dynamic *in situ* TXM measurements is required to fully elucidate the nucleation events of nanoparticles under  $\sim 50\ \text{nm}$  in size. With a better understanding of nucleation and growth of ZnO, films with improved crystallinity and various morphologies could be deposited for various optoelectronic applications. For example, the high contrast we observe in this work in the case of nanoplate films, is related to orientation of these structures, an important parameter for optimisation of the transport properties of these films for device applications. Further nucleation and growth studies of other systems could be investigated by *in situ* TXM, which obviates diffusion-limited constraints.

Use of the Stanford Synchrotron Radiation Lightsource, SLAC National Accelerator Laboratory, is supported by the U.S. Department of Energy, Office of Science, Office of Basic Energy Sciences under Contract No. DE-AC02-76SF00515. This work was funded in part by the EPSRC (EP/J500161/1). A.E.P acknowledges an ERC starting investigator grant (CNTBBB), A. E.G acknowledges support from an EPSRC Doctoral Prize Fellowship and S.E.R.T. is grateful to the Energy Innovation Programme Office, Singapore for his National Research Foundation (Clean Energy) Ph.D. scholarship.

## Notes and references

- 1 I. Gurrappa and L. Binder, *Sci. Technol. Adv. Mater.*, 2008, **9**, 043001.
- 2 J. E. Evans, K. L. Jungjohann, N. D. Browning and I. Arslan, *Nano Lett.*, 2011, **11**, 2809–2813.
- 3 T. J. Woehl, J. E. Evans, I. Arslan, W. D. Ristenpart and N. D. Browning, *ACS Nano*, 2012, **6**, 8599–8610.
- 4 Y. Liu, K. Tai and S. J. Dillon, *Chem. Mater.*, 2013, **25**, 2927–2933.
- 5 J. Grunwaldt and A. Baiker, *Phys. Chem. Chem. Phys.*, 2005, **7**, 3526–3539.
- 6 S. Fujii, D. Dupin, T. Araki, S. P. Armes and H. Ade, *Langmuir*, 2009, **25**, 2588–2592.
- 7 E. de Smit, I. Swart, J. F. Creemer, G. H. Hoveling, M. K. Gilles, T. Tylicszak, P. J. Kooyman, H. W. Zandbergen,

- C. Morin, B. M. Weckhuysen and F. M. F. de Groot, *Nature*, 2008, **456**, 222–225.
- 8 M. J. Williamson, R. M. Tromp, P. M. Vereecken, R. Hull and F. M. Ross, *Nat Mater*, 2003, **2**, 532–536.
  - 9 H. Zheng, R. K. Smith, Y.-W. Jun, C. Kisielowski, U. Dahmen and A. P. Alivisatos, *Science*, 2009, **324**, 1309–1312.
  - 10 J. Rieger, J. Thieme and C. Schmidt, *Langmuir*, 2000, **16**, 8300–8305.
  - 11 Y. G. Sun and Y. X. Wang, *Nano Lett.*, 2011, **11**, 4386–4392.
  - 12 J. Nelson, S. Misra, Y. Yang, A. Jackson, Y. Liu, H. Wang, H. Dai, J. C. Andrews, Y. Cui and M. F. Toney, *J. Am. Chem. Soc.*, 2012, **134**, 6337–6343.
  - 13 J. N. Weker, N. Liu, S. Misra, J. C. Andrews, Y. Cui and M. F. Toney, *Energy Environ. Sci.*, 2014, **7**, 2771–2777.
  - 14 B. N. Illy, A. C. Cruickshank, S. Schumann, R. Da Campo, T. S. Jones, S. Heutz, M. A. McLachlan, D. W. McComb, D. J. Riley and M. P. Ryan, *J. Mater. Chem.*, 2011, **21**, 12949–12957.
  - 15 B. N. Illy, B. Ingham and M. P. Ryan, *Cryst. Growth Des.*, 2010, **10**, 1189–1193.
  - 16 B. Ingham, B. N. Illy and M. P. Ryan, *J. Phys. Chem. C*, 2008, **112**, 2820–2824.
  - 17 B. Illy, Doctoral, Imperial College London, 2009.
  - 18 T. Pauporté and D. Lincot, *J. Electroanal. Chem.*, 2001, **517**, 54–62.
  - 19 B. Ingham, B. N. Illy, M. F. Toney, M. L. Howdyshell and M. P. Ryan, *J. Phys. Chem. C*, 2008, **112**, 14863–14866.
  - 20 D. Yebra, S. Kiil, C. Weinell and K. Dam-Johansen, *Prog. Org. Coat.*, 2006, **56**, 327–337.
  - 21 J. Cembrero and D. Busquets-Mataix, *Thin Solid Films*, 2009, **517**, 2859–2864.